Northumbria Research Link

Electrochemical Performance of Sandwich-like Porous Co_3O_4 Nanostructures on Nickel Foam

Bo Sun[a], Hui Zhang[a], Wenge Chen[a,1], Ahmed Elmarakbi[b], Yong-Qing Fu[b,z]

[a] School of Materials Science and Engineering, Xi'an University of Technology, Xi'an, Shaanxi, 710048, P.R. China

[b] Faculty of Engineering and Environment, Northumbria University, Newcastle upon Tyne, NE1 8ST, UK.

Abstract

Co_3O_4 is a good anode candidate for high-performance lithium ion batteries (LIBs), attributed to its high specific capacity. However, due to its poor conductivity and significant volume expansion during electrochemical reactions, electrochemical performance of Co_3O_4 electrode is quite poor for practical applications. Co_3O_4 electrodes with various micro-/nanostructures have been designed and synthesized but their performances are still unsatisfied. In this study, we propose and develop a novel sandwich type of Co_3O_4 nanostructures by adjusting the ratio of ammonium fluoride and urea during hydrothermal reactions. When this sandwich-like Co_3O_4 composite electrode was used as the electrode for LIBs, it retained an outstanding reversible capacity of 857 mAh g^{-1} after 70 cycles at a current density of 500 mA g^{-1}. When the current density was increased to 1000 mA g^{-1}, the reversible capacity was kept at 865 mAh g^{-1} with insignificant changes of its capacity.

Keywords: Morphological control; Sandwich-like Co_3O_4; Lithium ion batteries; Nickel foam

---

[1] Corresponding authors: Prof. Wenge Chen; Prof. Richard Yongqing Fu.
E-mail: wgchen001@263.net (W.G. Chen), richard.fu@northumbria.ac.uk (Y.Q. Fu)

Introduction

Lithium ion batteries (LIBs) are widely used in energy storage systems for electric vehicles and power supplies of various electronic equipment due to their high energy density, long cycle life and high efficiency.[1-4] However, currently used anode materials of LIBs (mainly graphite) have a relatively low theoretical capacity (e.g., 372 mAh g^{-1}), which cannot meet the stringent requirements of many applications. Therefore, it is critical to explore and develop new types of high-performance electrode materials.[5,6] In recent years, transition metal oxides (TMOs), such as Fe_2O_3, NiO, and CuO, etc., have been regarded as promising battery electrodes, attributed to their excellent physical and chemical properties.[7-9] Among them, Co_3O_4 is considered as a reliable electrode for the LIBs owing to its high theoretical capacity (up to 890 mAh g^{-1}), low cost and convenient preparation process.[10,11] However, Co_3O_4 has a poor conductivity and shows a large volume expansion during electrochemical reactions. These result in severe problems such as easily degraded microstructures, rapidly reduced currents and fast capacity decays, as well as poor cycling stability, all of which severely hinder its practical applications.[12,13]

Recently, great effort has been made to improve the electrochemical performance of Co_3O_4. One of the effective methods is to design and fabricate Co_3O_4 nanostructures with different morphologies, including nanorods, nanoneedles, and nanowalls,[14-16] whose highly porous and large specific surface areas can be effectively used to achieve high specific capacities. For example, Wang et al. prepared mesoporous Co_3O_4 nanorods using a hydrothermal method combined with diallyl dimethyl ammonium chloride assisted microstructures.[17] The initial capacity of the developed Co_3O_4 nanorods was 1343.8 mAh g^{-1} at a current density of 500 mA g^{-1}, and the capacity after 200 cycles was maintained at 74.7%, showing its excellent lithium-ion storage capacity and long-term cycling stability. Mule et al. fabricated three-dimensionally hexagonal plate-like Co_3O_4 arrays using a solvothermal method.[18] After 100 cycles, the capacity value (i.e., 606 mAh g^{-1}) was still maintained at 500 mA g^{-1}. Yang et al. synthesized ultrathin and two-dimensional Co_3O_4 nanosheets using a surfactant-assisted self-

assembly method.[19] At a current density of 100 mA g^{-1}, the capacity was as high as 1868.6 mAh g^{-1} after 30 cycles, and the capacity retention was close to 100%.

Another commonly used approach for improving the electrochemical performance of Co_3O_4 is to grow Co_3O_4 directly on the substrate of current collectors.[20,21] For example, Zhang et al. prepared mesoporous Co_3O_4 nanowires and nanosheets on the nickel foam using a hydrothermal method.[22] Among them, the reversible capacity of Co_3O_4 nanosheets was 1300 mAh g^{-1} after 100 cycles at a current density of 100 mAg^{-1} with a negligible decay of capacity. Xiong et al. grew Co_3O_4 nanowalls on surface of the nickel foam, and obtained a high reversible capacity of 835 mAh g^{-1}, which was maintained after 100 cycles at a current density of 200 mA g^{-1}.[23] Zhang et al. fabricated Co_3O_4 nanostructures with different morphologies on carbon cloth using a hydrothermal method.[24] At a current density of 1 A g^{-1}, the capacity was 621.8 F g^{-1}, which was maintained at 90.6% after 3000 cycles. Dai et al. synthesized porous Co_3O_4 nanosheet arrays on a cobalt foam using an *in-situ* redox method, and the as-prepared samples exhibited an ultrahigh capacitance of 2585 F g^{-1} at 5 mV s^{-1}.[25] It was still maintained a capacitance retention rate of 77.5% after 20,000 cycles at a current density of 5 A g^{-1}. Pan et al. used an electrochemical deposition method to prepare Co_3O_4 nanosheet arrays on a nickel foam framework and achieved an initial capacity of 6469 F g^{-1} at a current density of 5 mA cm^{-2}.[26]

To sum up, although various methods have been applied to improve the electrochemical properties of Co_3O_4 by modifying the morphology and structure of Co_3O_4 such as using nanorods and nanosheets, they have not effectively solved the key problems of volume expansion and low utilization of active materials. Therefore, the key issues for Co_3O_4 such as low rate capability and poor cycle performance have not been solved. On the other hand, selection of a suitable porous and conductive substrate for growing the Co_3O_4 is also very important for its applications, because this can help to improve its conductivity and provide physical and mechanical supports for its nanostructures.

In this paper, sandwich-like Co_3O_4 nanoarrays were grown on a nickel foam substrate using a hydrothermal method. This sandwich structure is composed of two

thicker Co_3O_4 layers with a few thin Co_3O_4 layers stacked in between. This type of sandwich structure can shorten the diffusion paths of lithium ions, increase the contact between electrode and electrolyte, and effectively form a buffer layer for accommodating large volume expansion in charge-discharge processes. The electrochemical performance of the fabricated sandwich-like Co_3O_4-Ni composite electrode was evaluated and a reversible capacity of 857 mAh g^{-1} was still maintained after 70 cycles at a current density of 500 mA g^{-1}, and it was 865 mAh g^{-1} when the current density was increased to 1000 mA g^{-1}.

Experimental

Synthesis of sandwich-like Co_3O_4 nanostructures on nickel foam. Sandwich-like Co_3O_4 nanostructures were synthesized using a hydrothermal synthesis method as illustrated in Fig. 1. Firstly, 4 mmol of $Co(NO_3)_2 \cdot 6H_2O$ was dissolved in 40 mL of water and stirred for 30 min to obtain a mixed solution. Then 20 mL of NH_4F aqueous solution (1.4 M) was added drop-wisely and stirred for 30 min, and this was followed by adding 10 mL of $CO(NH_2)_2$ aqueous solution (1.0 M) drop-wisely and stirring for another 30 min. A nickel foam substrate (size of 2cm×2cm×0.05cm with a porosity of 96~98%) was treated with a dilute hydrochloric acid solution (2 mol L^{-1}) and ethanol solution for removing surface impurities and oxides, respectively, before being used as the substrate for growing Co_3O_4 nanostructures. The above mixed solution was coated on the top of nickel foam, which was then transferred into a polytetrafluoroethylene stainless steel autoclave (with a filling ratio of 80%). This autoclave was kept at 180°C for 8 hours, and then naturally cooled down to room temperature. After this, the Co_3O_4 precursor grown on the nickel foam was washed with distilled water and ethanol for several times, and then dried at 60°C for 24 hrs. Finally, the obtained precursors were annealed at 300°C for 2 hrs with a heating rate of 5°C min^{-1} to obtain a black product, denoted as Co_3O_4-Ni electrode.

Material characterizations. Surface morphology and microstructure were characterized using a scanning electron microscope (SEM, ZEISS Sigma 300). Crystalline structures of the synthesized materials were studied using X-ray diffraction

(XRD, Bruker D8 ADVANCE) with Cu kα radiation. Chemical elements and their binding information were characterized using an X-ray photoelectron spectroscope (XPS, Thermo ESCALAB 250XI). A Raman spectroscope (Horiba Scientific LabRAM HR Evolution) was also used and excited using a laser beam with a wavelength of 532 nm.

Electrochemical characterizations. Electrochemical measurements of the synthesized materials were performed using a CR2032 coin type LIB. The Co_3O_4-Ni samples were cut into circular shaped discs and directly used as binder-free electrodes. The mass loading of Co_3O_4 on the nickel foam was ~4.2 mg/cm^2. A metallic Li foil was used as the counter/reference electrode. Polypropylene membrane (Celgard 2400) was used as the separator. The 1 M $LiPF_6$ was dissolved in a mixed solution of ethylene carbonate (EC), dimethyl carbonate (DMC), and diethyl carbonate (DEC), with a volume ratio 1:1:1, which was used as the electrolyte. The CR2032 coin type LIBs were assembled in an Ar-filled glove box. The galvanostatic charge-discharge (GCD) tests were performed at different currents with the potentials from 0.01 V and 3 V. Cyclic voltammograms (CV) tests were performed using an electrochemical analyzer (Bio Logic SP-150, France) at a scan rate of 0.1 mV s^{-1} in the potential range of 0.01 V to 3 V. The galvanostatic charge-discharge (GCD) tests of the assembled cells were performed with a voltage window of 0.01-3 V (vs Li/Li$^+$) using a battery testing system (LAND CT2001A) operated at room temperature. Cyclic voltammetry (CV) experiments were carried out using an electrochemical analyzer (Bio Logic SP-150).

Results and discussion

Fig. 2 shows the surface morphologies of Co_3O_4 prepared with different ratios of ammonium fluoride and urea. As shown in Fig. 2(a), nanowires of Co_3O_4 with an average diameter of 140 nm were obtained when the ratio of $NH_4F:CO(NH_2)_2$ was 8:10. Fig. 2(b) shows that when the ratio of $NH_4F:CO(NH_2)_2$ was increased to 10:10, the nanowires were adhered and bundled together, and their morphology was changed from separated nanowires into clusters of nanowires. As seen in Fig. 2(c), the nanowire clusters were then transformed into nanoribbons when the $NH_4F:CO(NH_2)_2$ ratio was

increased to 12:10. However, with the ratio of $NH_4F:CO(NH_2)_2$ further increased to 14:10, nanoribbons were observed at both sides of the substrate, and they were then transformed into the interwoven structures of nanosheets, as shown in Fig. 2(d).

Fig. 3 illustrates morphology evolutions of the sandwich-like Co_3O_4. In the hydrothermal environment, Co^{2+}, F^- and OH^- ions in the solution were diffused into the layered structure in two dimensions, whereas they were diffused onto the layer's surface along one dimension. Compared with the outer surface, the binding energy at the thin edge (i.e., the white area in Fig. 3) is higher and ions are easily adsorbed. Accordingly, the crystals are continually growing along this thin edge to form two surfaces of the sandwich structure. The compositions of these two layers should be the same. However, the upper and lower layers easily adsorb more ions, thus resulting in their increased thicknesses.

Fig. 4 shows the enlarged SEM images of Co_3O_4 grown on the nickel foam. Figs. 4(a) and 4(b) are SEM images of the nickel foam before and after coated with the sandwich-like Co_3O_4. Figs. 4(c) and 4(d) are SEM images of sandwich-like Co_3O_4 structures at different magnifications. Fig. 4(a) clearly shows that the surface of the nickel foam is very smooth before loaded with Co_3O_4. Fig. 4(b) shows that the skeleton of the nickel foam is covered with a layer of uniformly distributed Co_3O_4 nanostructure, formed after hydrothermal reactions. The nickel foam loaded with Co_3O_4 maintains its original three-dimensionally porous structure after the thermal oxidation process, indicating that the facile synthesis method has not damaged the structure of nickel foam. EDS analysis of the nickel foam loaded with Co_3O_4 is shown in the inset of Fig. 4(b). Its constituent elements of the prepared samples mainly include Co and O. A higher magnification SEM image is shown in Fig. 4(c), which reveals that the formed sandwich structure is composed of two thick layers of Co_3O_4 at both sides, with thinner multilayer Co_3O_4 structures stacked in the middle. Large-area sandwich-like nanostructures are uniformly grown on the surface of nickel foam. The outer layer thickness is 300 nm and each sublayer of the intermediate layer thickness is 30 nm. The internal pores of the layered structure are beneficial for the good contact of electrolytes and provide good contact at the interfaces between the electrode and the electrolyte in

this work.

XRD patterns of the Co_3O_4-Ni structures are shown in Fig. 5(a). The obtained diffraction peaks at the 2θ angles of 19.1°, 31.4°, 36.9°, 59.5°, and 65.4° are assigned to the crystallographic planes of the (111), (220), (311), (511), and (440) of Co_3O_4, respectively, which are well consistent with its cubic phase (JCPDS card no. 76-1802).[27,28] In addition, three peaks at the 2θ angles of 44.5°, 51.8°, and 76.3° are corresponding to the crystallographic planes of (111), (200), and (220) of nickel (JCPDS card no. 04-0850), which are mainly from the nickel foam substrate.[29] No other peaks are found in the XRD spectrum, indicating that only crystalline phase of Co_3O_4 was successfully synthesized on the nickel foam. XRD signal of Co_3O_4 is relatively weak, which is because the Co_3O_4 layer is very thin and the background signal of the nickel foam is too strong.

As shown in Fig. 5(b), the phases of the composite can be confirmed by Raman analysis results. For the cubic phase of Co_3O_4, Co^{2+} (3d ^{7}) and Co^{3+} (3d ^{6}) are combined with the oxygen at its tetrahedral and octahedral positions, respectively. The Raman spectrum of Co_3O_4 shows four peaks, located at ~691, ~523, ~484, and 194 cm^{-1}, respectively, which are consistent with the active modes of spinel phase Co_3O_4 according to the space group theory.[30] The Co^{2+}-O^{2-} vibrational mode (F_{2g}) at the tetrahedral sites shows a weak absorption band at 194 cm^{-1} whereas the Co^{3+}-O^{2-} vibrational mode (A_{1g}) at the octahedral sites shows a relatively strong absorption band at 691 cm^{-1}. Two absorption bands located at 484 and 523 cm^{-1} are ascribed to the combined vibrations of the cobalt-oxygen located at both tetrahedral and octahedral sites of the spinel phase Co_3O_4.[31]

Chemical and structural states of electrode materials were further studied using XPS. Fig. 5(c) shows the survey spectrum of the prepared sample, indicating the presence of Co 2p and O 1s peaks. Fig. 5(d) shows the high-resolution Co 2p spectrum, which can be deconvoluted into two peaks at 794.4 eV and 779.1 eV, corresponding to the spin orbit peaks of Co 2p$_{1/2}$ and Co 2p$_{3/2}$ of the Co_3O_4 phase, as well as the satellite peaks at 784.5 eV and 802.2 eV, respectively.[32] After deconvolution of the Co 2p peak, characteristic peaks of the Co^{3+} state were observed at 794.4 eV and 778.6 eV. Similarly,
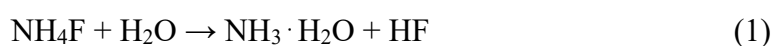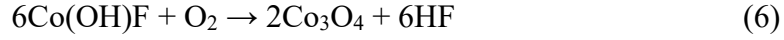
peaks corresponding to the Co^{2+} state are at 796.8 eV and 780.3 eV. The energy separation of 15.3 eV between these two peaks is a typical feature of Co_3O_4, which is due to spin orbit coupling effect.[33] The deconvolution results of spectra confirm the existence of Co^{3+} and Co^{2+} ions and the generation of phase Co_3O_4.

In the hydrothermal synthesis process, presence of NH_4F is essential for the formation of these homogeneously hierarchical structures.[34] NH_4F is easily decomposed into components of $NH_3 \cdot H_2O$ and HF in an aqueous solution. With the decomposition of $NH_3 \cdot H_2O$, OH^- is generated simultaneously. This will change the pH values of the precursor solution and reduce the acid contents of the precursor solution. Within the acidic environment, cobalt precursor in the aqueous solution is unstable and thus easily changed into low-dimensional nanostructures. The alkaline content in the precursor solution is mainly determined by the presence of NH_4^+, which can form a suitable environment and produce the Co(OH)F precursor. With the increase of concentration of NH_4F, the pH value of the precursor solution is increased, thus promoting the generation of 2D and 3D nanostructures. In addition, F^- ions are essential for the formation of lamellar structures, and they are easily chemisorbed by the dangling bonds. Therefore, they inhibit the growth of crystal planes due to their strong electronegativity values. This is the key reason why they have been widely used in the fields of crystal engineering and morphological tailoring.[35]

According to literature, morphology changes of anions are controlled by various factors, e.g., reducing the concentration of free ions,[36] adsorbing on specific crystal planes, or selectively etching desired crystal planes,[37] adjusting the pH value and ionic strength of the solution,[38] and forming intermediate products.[39] These effects have huge influences on the chemical kinetics of the reaction process, which results in the formation of different morphologies. The differences in their chemical kinetics are closely related to the contents of NH_4F during the reactions.

The chemical reactions, which involve the production of Co_3O_4 nanostructures,[18,22] can be written using equations (1)-(6):

$$NH_4F + H_2O \rightarrow NH_3 \cdot H_2O + HF \qquad (1)$$

$$NH_3 + H_2O \rightarrow NH_3 \cdot H_2O \leftrightarrow NH_4^+ + OH^- \tag{2}$$

$$H_2NCONH_2 + 3H_2O \rightarrow CO_2 + 2NH_4^+ + 2OH^- \tag{3}$$

$$Co^{2+} + F^- \rightarrow CoF^+ \tag{4}$$

$$CoF^+ + OH^- \rightarrow Co(OH)F \tag{5}$$

$$6Co(OH)F + O_2 \rightarrow 2Co_3O_4 + 6HF \tag{6}$$

According to the above reactions, the roles of F^- ions in the synthesis can be summarized as following:

(i) *The interaction between F^- and Co^{2+}.* As the concentration of NH_4F is increased, the formation of CoF^+ reduces the free concentration of Co^{2+} based on the Eq. (4), thereby reducing the reaction rate.

(ii) *Adjustment of solution pH value.* As the degree of hydrolysis of NH_4^+ is larger than that of F^-, with the increase of NH_4F's concentration, CoF^+ is more likely to combine with OH^- to form $Co(OH)F$, thus increasing the reaction rate.

(iii) *Ionic hydration of F^-.* Due to the effect of F^-, the water molecules in the solution will be trapped near F^-, thus inhibiting the movement of water molecules. It leads to the increase of the average activity coefficient of ions in the solution, thus increasing the reaction rate.

In this study, morphological control of the final products is regarded as synergistic effects of the above three reasons. With the increase of NH_4F, the morphology is changed from nanowires to nanoribbons, and finally to a sandwich-like structures. The controlled formation of Co_3O_4 with different morphologies can be realized by precisely controlling the NH_4F dosage.

In order to understand the electrochemical performance of lithium ions' insertion/extraction processes, CV measurements were carried out using sandwich-like Co_3O_4-Ni composite electrode, measured with a scanning rate of 0.1 mV s^{-1} in the potential range of 0.01 V to 3 V. Fig. 5(a) shows the first three cyclic voltammetry curves of the Co_3O_4-Ni composite electrode. It can be seen from Fig. 6(a) that as the potential is decreased, the reduction reaction of Co_3O_4 occurs. Therefore, the potential is gradually decreased and a peak of current is generated. With the further increase of the potential, the oxidation reaction occurs. Simultaneously the potential is increased

and an oxidation peak is formed, thus forming a complete cycle. The three prominent redox peaks at voltages of about 0.7 V, 1.1 V, and 2.1 V can be clearly observed, which are corresponding to the conversions among Co_3O_4 and Co, CoO, and Li_2O. During the initial cycle, the observed strong reduction peak at around 0.7 V corresponds to the initial reduction of Co_3O_4 into metallic cobalt and the formation of the solid electrolyte interface (SEI) film with the creation of amorphous Li_2O, i.e.,[40,41]

$$Co_3O_4 + 8Li^+ + 8e^- \rightarrow 3Co + 4Li_2O$$
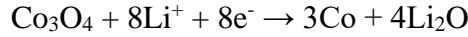
At the same time, there is a plateau at ~1.1 V and a broad oxidation peak at ~2.1 V, which should be caused by the oxidation of metallic cobalt into CoO and the decomposition of Li_2O, i.e.,[42,43]

$$Co + Li_2O \rightarrow CoO + 2Li^+ + 2e^-$$

Compared with the first cycle, the reduction peak of the second cycle is shifted significantly in the potential range of 0.7 V to 1.1 V, and the peak intensity is decreased significantly. The oxidation peak remains unchanged at 2.1 V. There phenomena are similar to those reported in literature.[44,45] It is worthwhile to note that the peak intensity and integral area of the third cycle are exactly the same as those of the second one, indicating that this composite electrode has both good electrochemical reversibility and cycling stability.

The charge-discharge measurements of the Co_3O_4-Ni composite electrode were performed in a potential range of 0.01 V to 3 V at different current rates. Fig. 6(b) presents the initial three cycles of the Co_3O_4-Ni composite electrodes at a current density of 100 mA g^{-1}. The initial discharge/charge capacity of the composite electrode is 1538 mAh g^{-1}/1089 mAh g^{-1}, respectively. During the initial discharge process, two distinct discharge plateaus were observed at around 1.1 V and 0.7 V due to the reduction of Co_3O_4 to metallic cobalt. There is a charging plateau around 2.2 V, which is related to the oxidation of Co, according to literature.[46] A large irreversible capacity was observed in the first cycle owing to the undesired reactions between the active material and the electrolyte, resulting in the formation of Li_2O on the surface of the electrode material with the accompanying SEI film generation.[40]

Furthermore, after the initial discharge, the subsequent cycling plateau is shifted

to the high potential side, which is in a good agreement with the CV results, indicating the occurrence of efficient Li-ion intercalation and deintercalation processes. The reversible capacity of the sample after three cycles is 1182 mAh g^{-1}. Compared with that of the pure Co_3O_4 (which has a reversible capacity of 420.5 mAh g^{-1}),[22] the as-prepared composite electrode has a much higher reversible capacity, indicating that direct growth of Co_3O_4 on the nickel foam substrate can improve the conductivity.

The cycle life of electrode materials is one of the important parameters for their excellent electrochemical properties. According to literature,[47-49] the cycle numbers of such materials are usually performed between 30 and 100 times. In this paper, cycling performance was carried out for 70 times at a current density of 500 mA g^{-1}, and the results are shown in Fig. 6(c). The initial discharge/charge capacity of the sample is 1685/1074 mAh g^{-1}. The initial irreversible capacity loss can be attributed to the formation of SEI film and decomposition of electrolyte, both of which are commonly occurred in metal oxide anodes.[50-52] The coulombic efficiency is ~65% for the first cycle, but this is rapidly increased to nearly 100% after the first six cycles. When the cycle numbers reaches 10 cycles, the capacity is increased slightly. This is mainly caused by incomplete activations of active materials or formation of uneven SEI film.[53,54] With the further increase of the number of cycles, the capacity remains nearly a constant. When the cycle number reaches 30 cycles, the capacity begins to decline slowly. This can be attributed to the collapse and agglomeration of the electrode material and the poor contact between the electrolyte and the electrode material.[40] The coulombic efficiency of the sandwich-like Co_3O_4-Ni electrode in this study can be maintained at 99% after 70 cycles, and a relatively high reversible capacity can still be maintained at 857 mAh g^{-1}. Results indicate that the prepared sandwich electrode material has shown a high charge-discharge efficiency. It is worthwhile to mention that the reversible capacity of the sample at the 70th cycle is nearly equal to the theoretical value of Co_3O_4.

Fig. 6(c) also shows the morphology and microstructures of sandwich-like Co_3O_4 electrode after cycling. It can be seen that the three-dimensional structure of the sandwich-like Co_3O_4 electrode after cycling remains intact. During the charge-

discharge process, the lamella structure became disappeared or covered with newly formed layers. However, the structure did not fall off or collapse. At the same time, the pores between the three-dimensional structures were remained. These pores were not only beneficial for adapting to the volume changes in the process of charge-discharge, but also advantageous to the transmission of lithium ions in the subsequent cycle. This shows that the sandwich-like Co_3O_4 nanostructures can withstand the insertion/extraction of lithium ions. Results confirm that during the charge-discharge process, the sandwich-like Co_3O_4 nanostructured electrode shows excellent electrochemical performance.

Table 1 summarizes the electrochemical performance of Co_3O_4 electrodes with different nanostructures reported in this study and those in literature. The 3D sandwich type of electrode composed of Co_3O_4-Ni in this study exhibits better electrochemical performance compared with many previously reported Co_3O_4 nanostructures as well as pure Co_3O_4. Excellent performance of the electrode is strongly dependent on the structure of the materials involved in the reaction process. This unique sandwich structure has layered networks formed by stacking of 30 nm thick multiple Co_3O_4 layer, with a large number of electrochemically active sites between these Co_3O_4 layers, which can maintain a good structural integrity. Based on this sandwich structure, Co_3O_4 can be accommodated to adapt to the large volume expansion and also cause shedding effect in the charge-discharge processes, thereby improving the cycle stability.

Meanwhile, the lamella thickness of Co_3O_4 is closely related to the diffusion time ($t = x^2/2D$), where t is the diffusion time, x is the diffusion distance, and D is the diffusion coefficient.[58] Since the performance of the electrode depends on the simultaneous transport of lithium ions and electrons to the redox-active interface, reducing the size of the anode structure significantly reduces the diffusion time according to the above formula. Furthermore, the layered porous structure composed of stacked sheet structures allows the electrolyte to easily penetrate into the inner sheet and the inner multilayer structures, thus effectively increasing their reversible capacity. This is because this specially designed 3D sandwich nanostructures could increase the contact areas between the active material and the electrolyte, not only providing more

active centers, but also shortening the transmission paths of electrons and lithium ions.

The rate capability of the electrode was further evaluated at different current densities from 100 to 1000 mA g^{-1}. Fig. 6(d) demonstrates the rate capability of the sandwich-like Co_3O_4-Ni composite electrode. Their reversible capacities are maintained at 1234, 1155, 1036, 865 mAh g^{-1} when the current densities are 100, 200, 500, and 1000 mA g^{-1} (each for 10 cycles), respectively. When the current density is changed back to 100, 200, and 500 mA g^{-1} again, the reversible capacities reach 1213, 1114, and 975 mAh g^{-1}, respectively. Fig. 6(d) shows that the reversible capacity is decreased as the current density is increased from 100 mA g^{-1} to 1000 mA g^{-1}, and then increased as the current density is decreased to 100 mA g^{-1}.

The decrease in reversible capacity may be due to the shortened charge-discharge time at a large current density, and the lower diffusion rate of Li ions and electrons caused by the poor conductivity of Co_3O_4, thus resulting in a lower utilization of active materials. Subsequently, when the current density is decreased, the reversible capacity is decreased. However, the decreasing magnitude is not large, demonstrating that the electrode material can withstand different intensities of charge-discharge currents with a good rate performance. After 70 cycles, the reversible capacity is still maintained at 1203 mAh g^{-1} when the current density is 100 mA g^{-1}.

The excellent rate capability of the electrode is due to the unique morphology of the sandwich-like Co_3O_4, which has good surface permeability. Not only can it provide a shorter diffusion path for lithium ions' diffusion, but also it can promote the penetration of the electrolyte and facilitate the contact between the active material and the electrolyte. The sandwich structure composed of the nanoplates can make it easier to adapt to drastic volume changes and effectively keep the electrolytes during Li-ion insertion/extraction processes at a high current density.

Results in Fig. 7 show that reversible capacity of the sandwich-like Co_3O_4-Ni is much larger than that of pure Co_3O_4 at the same current rate, which indicates that the Co_3O_4 sandwich nanostructures on the nickel foam can achieve a much higher capacity. To compare the electrochemical performance of the electrode materials in this study with those reported in literature, the rate capability of the sandwich-like Co_3O_4-Ni in

this study and those of the Co_3O_4 based electrode materials with different morphologies are shown in Fig. 7.[19,22,23,46,55,57,59] It can be seen that the rate capability of the as-prepared sandwich-like composite electrodes in this study is better than most of those reported Co_3O_4-based anode materials in literature. Regarding to the effects of electrode structures, although the transmission efficiency of lithium ions and electrons for those three-dimensional electrode structures is not as good as that of two-dimensional and one-dimensional structures, three-dimensional structures can effectively avoid the easy fracture and peeling-off. These failures often occur in two-dimensional and one-dimensional structures, mainly due to the significant volume changes during the repeated cycles. The 3D sandwich-like structure also shows a good adhesion to the substrate, which can improve the overall stability and prevent the agglomeration of active materials.

The properties of sandwich Co_3O_4 structures are then further compared with those of other nanostructures of Co_3O_4. If compared with one-dimensional structure such as nanowires, the stability of three-dimensional structure is higher, although sandwich like three-dimensional structure is not as fast as one-dimensional structure in lithium ion and electron transport. It is well-known that the one-dimensional structure is easy to break or fall off due to volume expansion in the process of charge-discharge, which affect its electrochemical performance and service life time. For example, as reported in the literature,[59] the capacity of nanowires Co_3O_4 can reached 1193 mAh/g at low current density (100 mA/g). However, with the increase of current density, the capacity decreases gradually, and the cycling performance becomes much poorer. The three-dimensional structure can effectively avoid the structural damage caused by volume expansion and ensure the structural integrity of active materials. In addition, agglomeration of active materials can be avoided using these 3D structures. Compared with one-dimensional structure, the open space between layers of 3D structures improves the stability of the whole structure during the charge-discharge cycle, which adapts well with the large volume change.

The capacity of two-dimensional nanosheets Co_3O_4 is very high at low current density, but it decays rapidly with the increase of current density. As reported in Ref.

19, nanosheets of Co_3O_4 maintained the capacity of 1868 mAh/g after cycling at 100 mA/g, but its capacity was decreased significantly with the increase of current density or cycling numbers. Although two-dimensional structures, such as nanosheets, can also increase the contact areas between the electrode and the electrolyte, the three-dimensional structure has a much higher utilization of active materials than those of two-dimensional structures, because these three-dimensional structures contact well with the electrolyte, and can form a good conductive network. In addition, it can prevent the agglomeration of active materials. The sandwich-like three-dimensional structure formed by stacking layers can also promote the rapid transmission of lithium ions and electrons through the multi-layers, and shorten the diffusion path. Therefore, we can confirm that the good performance of sandwich Co_3O_4 electrode is attributed to its unique three-dimensional structure.

The novel sandwich-like structure leads to excellent electrochemical performance of Li-ion batteries, and we have identified three main reasons. (i) This sandwich structure shortens the diffusion paths of Li ions and electrons, facilitates the rapid transport of Li ions and electrons, and improves the utilization of Co_3O_4 active materials. (ii) The three-dimensional interlayer networks not only accommodate the volume expansion and avoid the spallation during the charge-discharge processes, but also ensure the integrity of the structure and prevent the agglomeration of active materials. (iii) Increasing the contact area at the electrode-electrolyte interface improves the mass transfer, which is beneficial for the enhancement of diffusion kinetics.

Conclusions

In summary, sandwich-like Co_3O_4-Ni composite electrodes were prepared using the raw materials of ammonium fluoride, urea and cobalt nitrate, with the nickel foam as the substrate. The hydrothermal reaction was done at 180°C for 8 h with a ratio $NH_4F:CO(NH_2)_2$ of 14:10. For the sandwich structure, the thickness of the Co_3O_4 outer layer was 300 nm and the thickness of the Co_3O_4 middle layer was 30 nm, which shortens the diffusion paths of Li ions and electrons, accommodates the volume expansion during the charge-discharge processes, and increases the contact area at the

electrode-electrolyte interface. The as-prepared Co_3O_4-Ni composite electrode material achieved a reversible capacity of 1074 mAh g^{-1} at 500 mA g^{-1}, and a capacity retention rate of about 79.8% after 70 cycles. When the current density was 100 mA g^{-1}, the reversible capacity was still maintained at 1203 mAh g^{-1}.

Acknowledgments

ORCID

Wenge Chen https://orcid.org/0000-0003-3842-2914
Richard Yongqing Fu http://orcid.org/0000-0001-9797-4036

References

1. A. S. Mussa, M. Klett, M. Behm, G. Lindbergh, and R.W. Lindström, *J. Energy Storage*, **13**, 325 (2017).
2. A. Vlad, N. Singh, J. Rolland, S. Melinte, P. M. Ajayan, and J.-F. Gohy, *Sci. Rep.*, **4**, 4315 (2014).
3. J. W. Choi, and D. Aurbach, *Nat. Rev. Mater.*, **1**, 16013 (2016).
4. Y. Qiao, K. Z. Jiang, H. Deng, and H. S. Zhou, *Nat. Catal.*, **2**, 1035 (2019).
5. A. Eftekhari, *Energy Storage Mater.*, **7**, 157 (2017).
6. J. Lu, Z. W. Chen, F. Pan, Y. Cui, and K. Amine, *Electrochem. Energy Rev.*, **1**, 35 (2018).
7. D. Narsimulu, G. Nagaraju, S.C. Sekhar, B. Ramulu, S.K. Hussain, and J. Yu, *J. Alloys Compd.*, **846**, 156385 (2020).
8. Y. Lu, L. Yu, and X. W. Lou, *Chem*, **4**, 972 (2018).
9. J. Li, S. Y. Hwang, F. M. Guo, S. Li, Z. W. Chen, R. H. Kou, K. Sun, C.-J. Sun, H. Gan, A. P. Yu, E. A. Stach, H. Zhou, and D. Su, *Nat. Commun.*, **10**, 2224 (2019).
10. D. M. Yin, G. Huang, Q. J. Sun, Q. Li, X. X. Wang, D. X. Yuan, C. L. Wang, and L. M. Wang, *Electrochim. Acta*, **215**, 410 (2016).
11. M. Cheng, S. B. Duan, H. S. Fan, X. R. Su, Y. M. Cui, and R. M. Wang, *Chem. Eng. J.*, **327**, 100 (2017).
12. P. M. Ette, P. Gurunathan, and K. Ramesha, *J. Power Sources*, **278**, 630 (2015).
13. Y. Wang, R. T. Guo, W. Liu, L. H. Zhu, W. B. Huang, W. Wang, and H. H. Zheng, *J. Power Sources*, **444**, 227260 (2019).

14. G. Y. Huang, S. M. Xu, S. S. Lu, L. Y. Li, and H. Y. Sun, *Electrochim. Acta*, **20**, 420 (2014).

15. L. L. Jin, X. W. Li, H. Ming, H. H. Wang, Z. Y. Jia, Y. Fu, J. Adkins, Q. Zhou, and J. W. Zheng, *RSC. Adv.*, **4**, 6083 (2014).

16. J. Z. Yin, R. Q. Li, Z. H. Sheng, Q. Q. Li, P. S. Zhao, Z. P. Cheng, L. L. Zhang, and Z. J. Jiang, *Mater. Lett.*, **233**, 122 (2018).

17. B. Wang, S. F. Wang, Y. Y. Tang, Y. X. Ji, W. Liu, and X. Y. Lu, *Energy Proc.*, **158**, 5293 (2019).

18. A. R. Mule, D. Narsimulu, A. K. Kakarla, and J. S. Yu, *Appl. Surf. Sci.*, **551**, 148942 (2021).

19. J. Yang, M. Z. Gao, J. F. Lei, X. J. Jin, L. Yu, and F. F. Ren, *J. Solid State Chem.*, **274**, 124 (2019).

20. P. Zhang, Z. P. Guo, S. G. Kang, Y. J. Choi, C. J. Kim, K. W. Kim, and H. K. Liu, *J. Power Sources*, **189**, 566 (2009).

21. D. Golodnitsky, M. Nathan, V. Yufit, E. Strauss, K. Freedman, L. Burstein, A. Gladkich, and E. Peled, *Solid State Ionics*, **177**, 2811 (2006).

22. Y. Q. Zhang, Y. W. Wu, Y. H. Chu, L. Li, Q. P. Yu, Y. F. Zhu, G. Liu, Q. Hou, R. H. Zeng, and L. Z. Zhao, *Electrochim. Acta*, **188**, 909 (2016).

23. L. Z. Xiong, Y. Teng, Y. X. Wu, J. J. Wang, and Z. Q. He, *Ceram. Int.*, **40**, 15561 (2014).

24. H. F. Zhang, C. X. Lu, H. Hou, Y. Y. Ma, and S. X. Yuan, *J. Alloys Compd.*, **797**, 970 (2019).

25. Y. M. Dai, S. S. Zhu, C. C. Wang, Y. Cong, Y. H. Zeng, T. T. Jiang, H. H. Huang, S. H. Huang, and X. K. Meng, *J. Alloys Compd.*, **748**, 291 (2018).

26. X. X. Pan, X. M. Chen, Y. Li, and Z. N. Yu, *Electrochim. Acta*, **182**, 1101 (2015).

27. H. Shan, N. Padmanathan, D. McNulty, C. O'Dwyer, and K. M. Razeeb, *ACS Appl. Mater. Interfaces*, **8**, 28592 (2016).

28. J. Y. Zhang, S. W. Wang, and G. B. Xu, *J. Alloys Compd.*, **856**, 158110 (2021).

29. X. Y. Hu, X. M. Tian, Y. W. Lin, and Z. H. Wang, *RSC Adv.*, **9**, 31563 (2019).

30. M. Aadil, M. F. Warsi, P. O. Agboola, M. F. A. Aboud, and I. Shakir, *Ceram. Int.*, **47**, 9008 (2021).

31. P. M. Ette, K. Selvakumar, S. M. S. Kumar, and K. Ramesha, *Electrochim. Acta*, **310**, 184 (2019).

32. G. Wei, L. Yan, H. F. Huang, F. X. Yan, X. Q. Liang, S. K. Xu, Z. Q. Lan, W. Z. Zhou, and J. Guo, *Appl. Surf. Sci.*, **538**, 147932 (2021).

33. A. Ali, M. Ammar, I. Hameed, M. Ali, M. Tayyab, R. Mujahid, I. Ali, M. Zia-ul-Haq, and M. Ashraf, *J. Electrochem. Soc.*, **167**, 100509 (2020).

34. S. K. Hussain, and J. S. Yu, *Chem. Eng. J.*, **361**, 1030 (2019).

35. F. F. Wu, X. J. Ma, J. K. Feng, Y. T. Qian, and S. L. Xiong, *J. Mater. Chem. A*, **2**, 11597 (2014).

36. C. Y. Liu, Y. F. Chen, H. Huang, C. X. Duan, X. Z. Ma, G. J. Wang, J. Luo, H. C. Luo, and J. L. Li, *Electrochim. Acta*, **416**, 140281 (2022).

37. Y. T. Dai, Y. Meng, J. G. Wang, S. Liu, S. Li, Y. Y. Li, K. Wang, and Z. P. Li, *Colloids Surf., A*, **627**, 127216 (2021).

38. S. T. Pei, S. Y. Ma, X. L. Xu, O. Almamoun, Y. T. Ma, and X. H. Xu, *J. Alloys Compd.*, **859**, 158400 (2021).

39. N. Tripathy, K. C. Das, S. P. Ghosh, D. Pradhan, and J. P. Kar, *Ceram. Int.*, **45**, 23993 (2019).

40. J. C. Zheng, and B. Zhang, *Ceram. Int.*, **40**, 11377 (2014).

41. X. Y. Xue, S. Yuan, L. L. Xing, Z. H. Chen, B. He, and Y. J. Chen, *Chem. Commun.*, **47**, 4718 (2011).

42. L. Zhan, S. Q. Wang, L. X. Ding, Z. Li, and H. H. Wang, *Electrochim. Acta*, **135**, 35 (2014).

43. Z. T. Cui, S. G. Wang, Y. G. Zhang, and M. H. Cao, *Electrochim. Acta*, **182**, 507 (2015).

44. H. R. Du, C. Yuan, K. F. Huang, W. H. Wang, K. Zhang, and B. Y. Geng, *J. Mater. Chem. A*, **11**, 5 (2017).

45. M. J. Jing, M. J. Zhou, G. Y. Li, Z. G. Chen, W. Y. Xu, X. B. Chen, and Z. H. Hou, *ACS Appl. Mater. Interfaces*, **11**, 9662 (2017).

46. J. Y. Cheong, J. H. Chang, S. H. Cho, J. W. Jung, C. H. Kim, K. S, Dae, J. M. Yuk, and I. D. Kim, *Electrochim. Acta* **295**, 7 (2019).

47. G. Huang, F. F. Zhang, X. C. Du, Y. L. Qin, D. M. Yin, and L. M. Wang, *ACS Nano*, **9**, 1592 (2015).

48. D. L. Wang, Y. C. Yu, H. He, J. Wang, W. D. Zhou, and H. D. Abruña, *ACS Nano*, **9**, 1775 (2015).

49. J. Y. Xiao, Z. X. Zhu, G. Q. Zhang, H. Y. Li, Y. L. Li, X. Z. Ren, P. X. Zhang, and H. W. Mi, *Appl. Surf. Sci.*, **545**, 149022 (2021).

50. M. Zhang, Z. P. Deng, X. F. Zhang, L. H. Huo, and S. Gao, *J. Alloys Compd.*, **863**, 158772 (2021).

51. J. X. Wang, Q. B. Zhang, X. H. Li, D. G. Xu, Z. X. Wang, H. J. Guo, K. L. Zhang, *Nano Energy*, **6**, 19-26 (2014).

52. X. W. Lou, D. Deng, J. Y. Lee, J. Feng, and L. A. Archer, *Adv. Mater.*, **20**, 258-262 (2008).

53. S. L. Xiong, J. S. Chen, X. W. Lou, and H. C. Zeng, *Adv. Funct. Mater.*, **22**, 861-871 (2012).

54. B. Zhang, Y. Zhang, Z. Miao, T. Wu, Z. Zhang, and X. Yang, *J. Power Sources*, **248**, 289-295 (2014).

55. L. Li, K.H. Seng, Z. Chen, Z. Guo, and, H.K. Liu, *Nanoscale*, **5**, 1922-1928 (2013).

56. W. P. Wang, M. S. Zhang, R. Y. Mi, Y. G. Liu, and J. Chen, *J. Alloys Compd.*, **888**, 161615 (2016).

57. Y. G. Liu, H. C. Wan, N. Jiang, W. X. Zhang, H. Z. Zhang, B. D. Chang, Q. Wang, Y. H. Zhang, Z. Y. Wang, S. H. Luo, and H. Y. Sun, *Solid State Ionics*, **334**, 117 (2019).

58. S. M. Xu, C. M. Hessel, R. Hao, R. B. Yu, Q. Jin, Y. Mei, H. J. Zhao, and W. Dan, *Energy Environ. Sci.*, **7**, 632 (2014).

59. M. M. Liang, M, S. Zhao, H. Y. Wang, F. Wang, and X. P. Song, *J. Energy Storage*, **17**, 311 (2018).

Tables

Table 1. Performance comparison of Co_3O_4 nanostructures as anode materials for lithium-ion batteries

| Samples and refs.	Current dentsity mA g^{-1}	Reverible capacity mA h g^{-1}	Cycle life
Co_3O_4 nanorods[17]	500	733.9 / 200th	74.7% retention / 200th
Bowknot-like Co_3O_4[44]	178	1389 / 100th	75.4% retention / 100th
Co_3O_4 rose-spheres[45]	90	1110 / 50th	67.9% retention / 50th
Hierarchical Co_3O_4[55]	100	1448 / 80th	105.2% retention / 80th
Co_3O_4 nanosheets[56]	200	1502.5 / 100th	97.8 retention / 100th
Co_3O_4 nanocubes[57]	100	873.5 / 50th	98.3% retention / 50th
Co_3O_4 nanowalls[23]	200	835 / 100th	74.2% retention / 100th
Co_3O_4-Ni[18]	500	606 / 100th	42.7% retention / 100th
Pure Co_3O_4[47]	100	420.5 / 100th	47.7% retention / 100th
This work	500	857 / 70th	79.8% retention / 70th

Figures
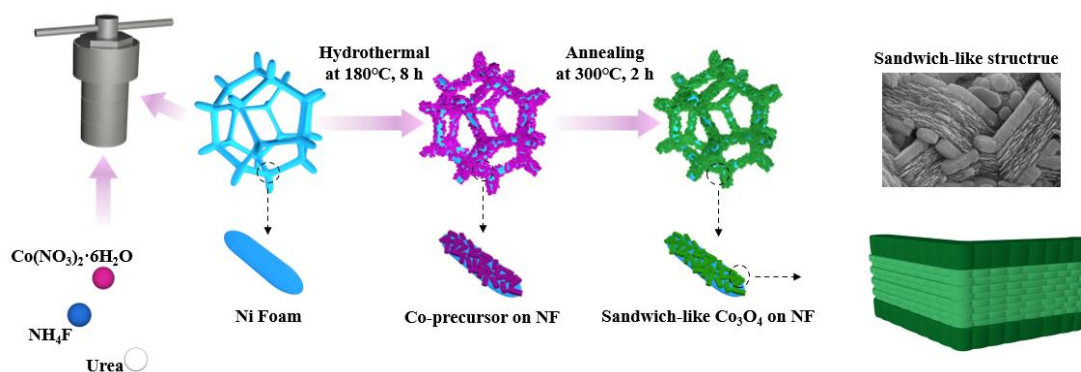
**Figure 1.** Schematic illustrations of the fabrication processes of sandwich-like Co_3O_4 on nickel foam
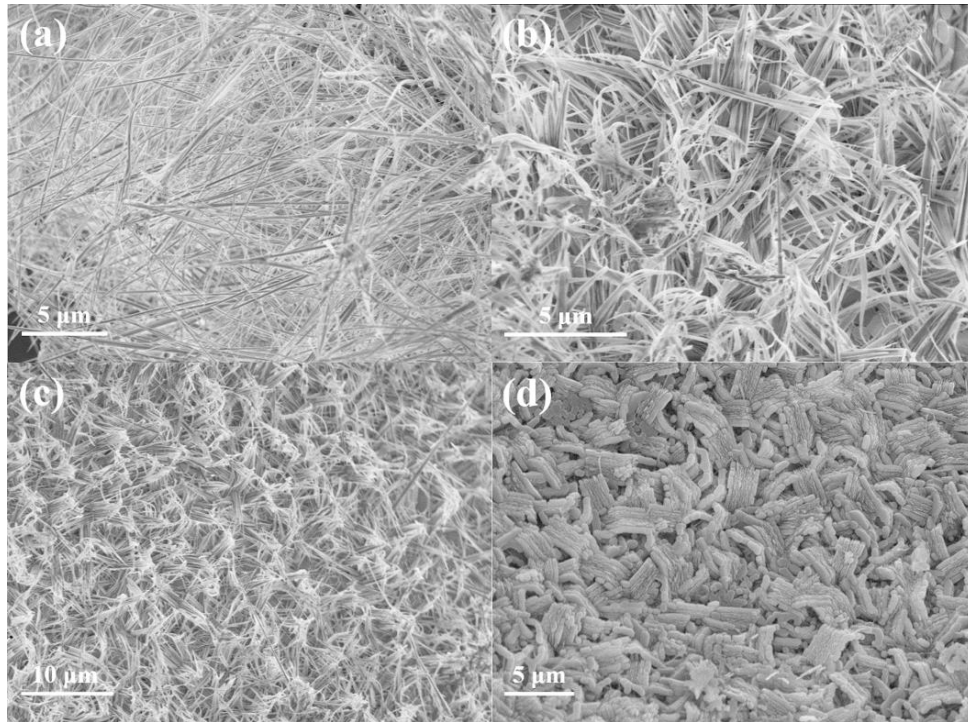
Figure 2. Micromorphology of Co_3O_4 with different ratios of ammonium fluoride and urea: (a) 8:10, (b) 10:10, (c) 12:10 and (d) 14:10.
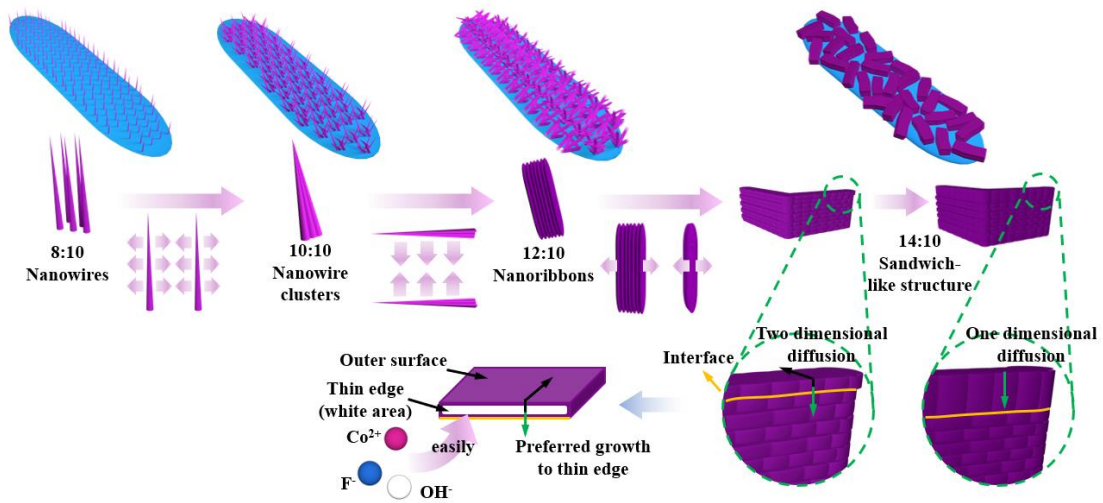

Figure 3. Illustrations of evolution of sandwich-like Co_3O_4.
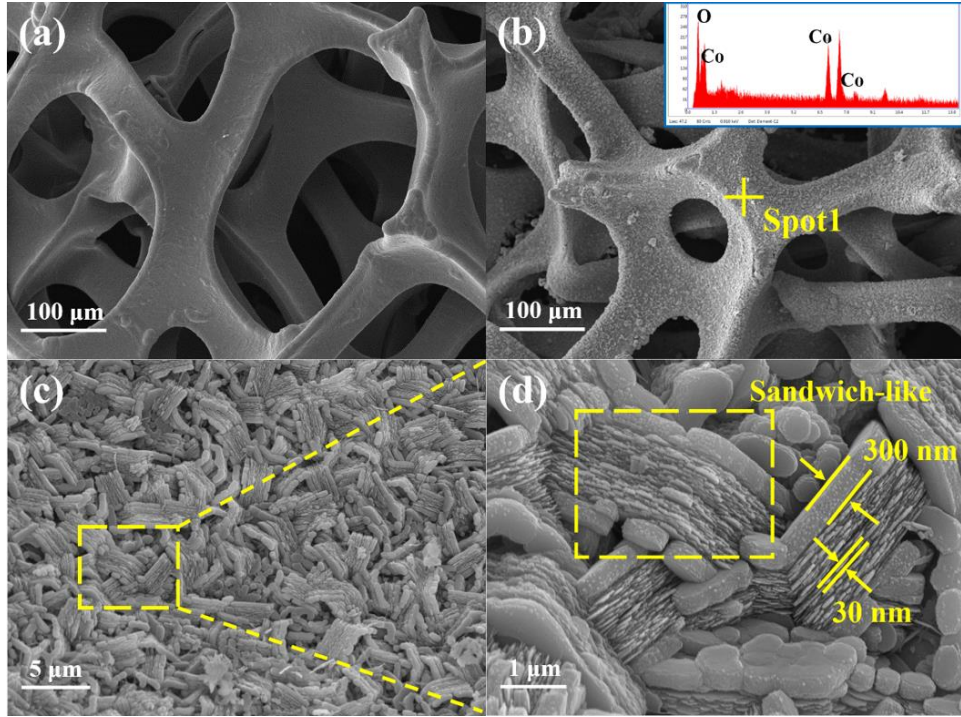
**Figure 4.** SEM images of Co₃O₄-Ni: (a-b) SEM image of the nickel foam before and after growing sandwich-like Co₃O₄ and EDS spectrum of sandwich-like Co₃O₄ on nickel foam; and (c-d) high-magnification images of the sandwich-like Co₃O₄ on nickel foam.
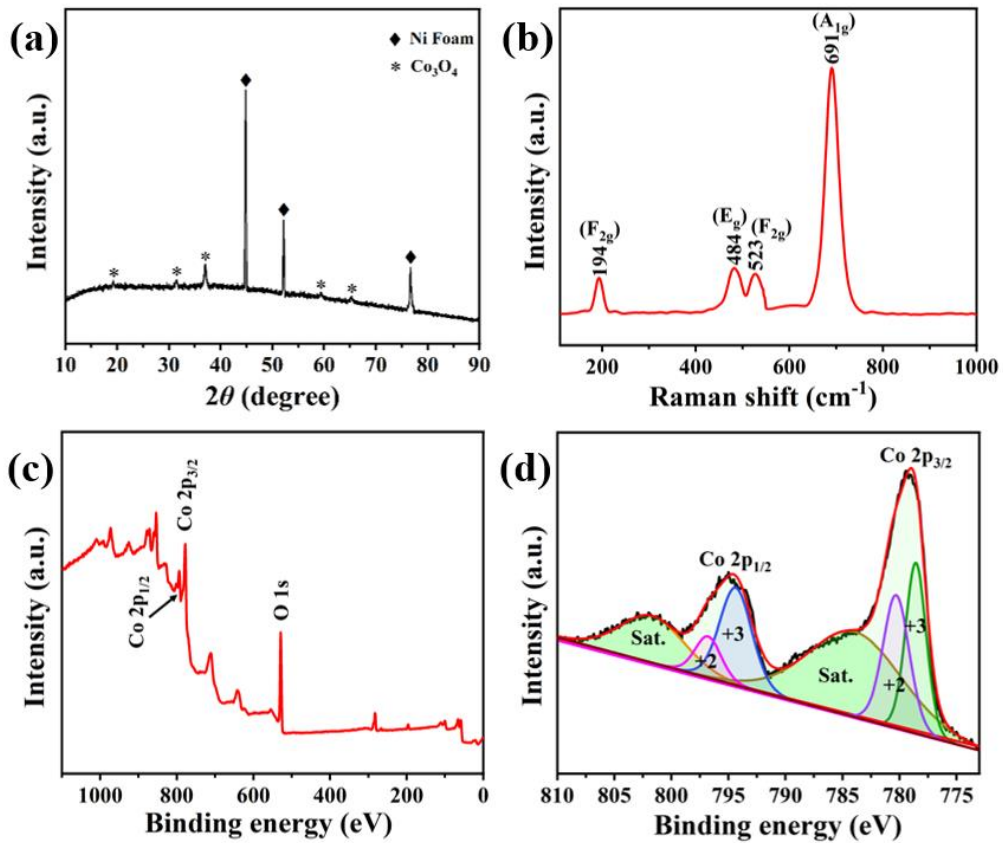
Figure 5. (a) XRD patterns of the Co_3O_4-Ni. (b) Raman spectra of the Co_3O_4-Ni. (c) survey and

(d) Co 2p XPS spectra of the Co_3O_4-Ni.
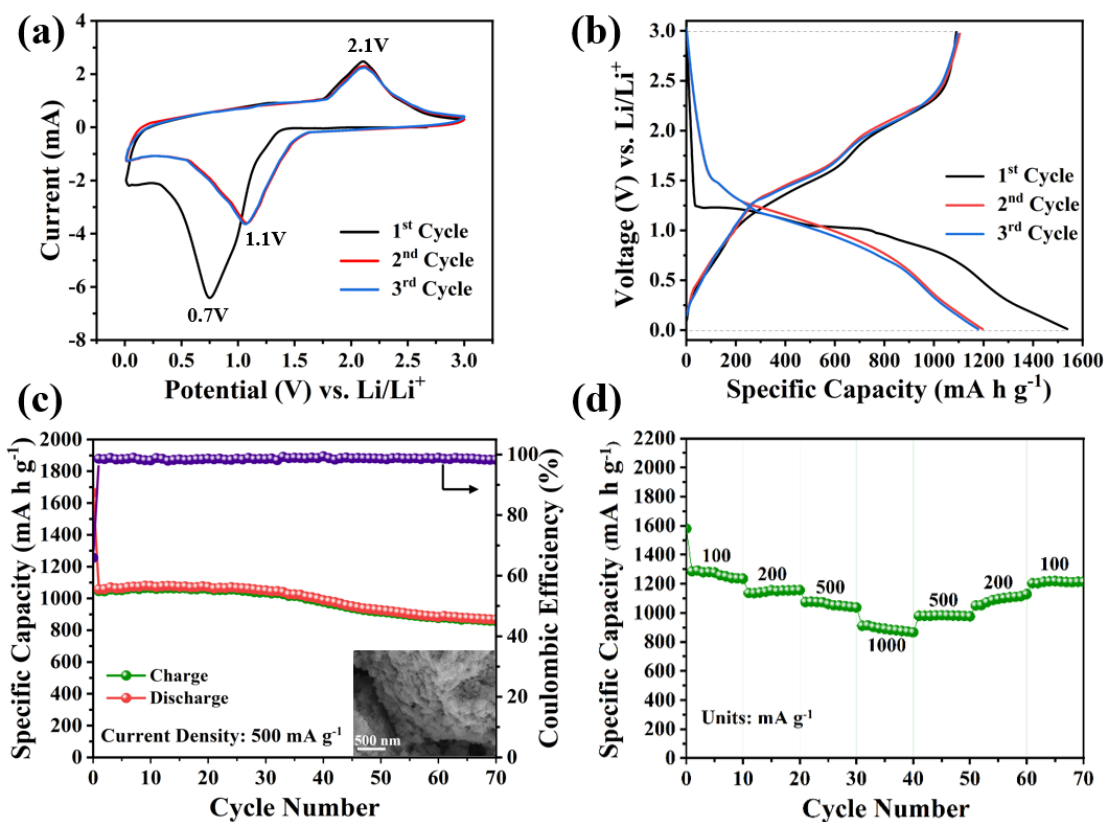
Figure 6. (a) The CV curves of the Co_3O_4-Ni composite electrode. (b) The GCD curves of the

Co_3O_4-Ni composite electrode; (c) The cycling performance of the Co_3O_4-Ni composite electrode

at a current density of 500 mA g^{-1}. The inset is the sandwich-like Co_3O_4 nanostructures after

cycling. (d) The rate capability of the Co_3O_4-Ni composite electrode at different current densities.
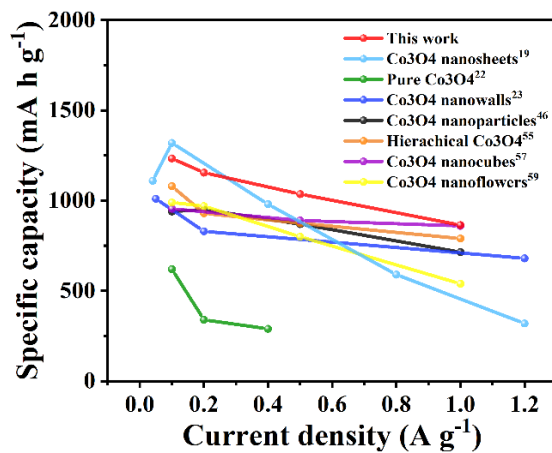
Figure 7. Comparison of rate performance of different Co_3O_4 nanostructure electrodes.